PAPER

Check for updates

A simple decagram-scale synthesis of an atomically dispersed, hierarchically porous Fe–N–C catalyst for acidic ORR†

Burak Koyuturk,‡[a] Eliyahu M. Farber, ID ‡[b] Friedrich E. Wagner,[c] Tim-Patrick Fellinger ID *[ad] and David Eisenberg ID *[b]

Carbons doped with iron and nitrogen (Fe–N–Cs) are highly promising electrocatalysts for energy conversion reactions in the oxygen, nitrogen and carbon cycles. Containing no platinum group metals, they nevertheless compete with platinum-based catalysts in crucial fuel cell reactions, such as oxygen reduction in acid. Yet deployment of Fe–N–Cs in fuel cells requires also a flow-enhancing pore structure, and a scalable synthesis procedure – a rarely-met combination of requirements. We now report such a simple synthesis of over 10 g of an Fe–N–C catalyst with high activity towards oxygen reduction in acid. Atomically-dispersed Fe–N$_4$ active sites were designed orthogonally and simultaneously with hierarchical micro-, meso- and macroporosity, by exploiting a dual role of magnesium ions during pyrolysis. Combining the "active site imprinting" and "self-templating" strategies in a single novel magnesium iminodiacetate precursor yielded a catalyst with high specific surface area (SSA > 1600 m^2 g^{-1}), a flow-enhancing hierarchical porosity, and high relative abundance of the most desirable D1-type Fe–N$_4$ sites (43%, by Mössbauer spectroscopy at 4.2 K). Despite the relatively low iron contents, the catalysts feature halfwave potentials up to 0.70 V *vs.* RHE at pH 1 and a mass activity of 1.22 A g^{-1} at 0.8 V *vs.* RHE in RDE experiments. Thanks to the simple and scalable synthesis, this active and stable catalyst may serve as a workhorse in academic and industrial research into atomically-dispersed ORR electrocatalysis.

[a]*Chair of Technical Electrochemistry, Department of Chemistry and Catalysis Research Center, Technical University of Munich, Lichtenbergstraße 4, D-85748 Garching, Germany*

[b]*Schulich Faculty of Chemistry, Grand Technion Energy Program, Russell Berrie Nanotechnology Institute, Technion–Israel Institute of Technology, Technion City, Haifa, 3200003, Israel. E-mail: eisenberg@technion.ac.il*

[c]*Department of Physics, Technical University of Munich, D-85748 Garching, Germany*

[d]*Bundesanstalt für Materialforschung und -prüfung (BAM), Unter den Eichen 44-46, 12203 Berlin, Germany. E-mail: tim-patrick.fellinger@bam.de*

† Electronic supplementary information (ESI) available. See https://doi.org/10.1039/d2ta00925k

‡ These authors contributed equally and may switch the order of their names when listing their publications.

Tim Fellinger studied the interdisciplinary course of "nanostructure and molecular sciences" and was privileged with the direct PhD supervision of Prof. Markus Antonietti (2009–2011). His materials chemistry background was shaped in the creative environment of the Max-Planck-Institute of Colloids and Interphases, where he also started his independent career in 2013. His scientific vision is to tailor nanostructured carbon-based materials to be able to transfer biochemical principles targeting electro-chemical energy applications, earning him the Ernst-Haage Price for Chemistry 2018. He was further educated and influenced by Prof. Hubert Gasteiger, who hosted his group 2017 to 2020 at TUM. Since 2020 he established his research group at BAM.

This journal is © The Royal Society of Chemistry 2022

J. Mater. Chem. A, 2022, **10**, 19859–19867 | **19859**

Introduction

Proton-exchange-membrane fuel cells (PEMFCs) are efficient and clean power devices, an integral part of the vision of clean and sustainable energy economy. Electric PEMFC-powered vehicles running on carbon-neutral fuels (*e.g.* green hydrogen[1]) can help cut CO_2 emissions and reduce our reliance on fossil fuels.[2,3] To make PEMFCs commercially viable, the cathode catalysts for the oxygen reduction reaction (ORR) must use as little platinum group metals (PGMs) as possible.[4,5] Research into PGM-free ORR electrocatalysts began in 1964, when Jasinski reported molecular cobalt phthalocyanine to be active towards the ORR in alkaline medium.[6] Recent years have witnessed an exponential increase in the number of heterogeneous ORR electrocatalysts, based on carbon and either free or low in PGMs.[7–13] Lately, single atom catalysts (SACs) have emerged as a new frontier in ORR electrocatalysis research.[14–19] Containing atomically dispersed, heteroatom-coordinated metals (*e.g.* Fe–N$_4$) on a conductive carbon matrix, such materials exhibit outstanding ORR activity and selectivity in acid and alkaline media in comparison to other PGM-free catalysts.[18–26]

To translate the promise of SACs into practical fuel cell cathodes, highly active catalytic sites are not enough.[27] First, to achieve high power density, the reactants and products must move fast through the material. This calls for hierarchically porous carbons, combining high surface areas for active site exposure, with a network of flow-enabling larger pores.[28] Second, the materials must be synthesized reproducibly and in large quantity, to enable extensive fundamental investigations and to allow for commercial scale-up. Most current syntheses of Fe–N–C SACs yield catalytic powders on the ten milligram scale,[12,18,20,21,29–36] whereas a hundred gram scale is needed to power automotive fuel cell stacks at current performance levels.[37–39] Large scale syntheses of Fe–N–C materials have been reported recently,[40,41] albeit relying on commercial activated carbons, rich in micropores yet lacking significant flow-enhancing meso- or macroporosity. To the best of our knowledge, the only hierarchically porous, atomically dispersed Fe–N–C commercially produced on a gram scale is the proprietary material developed by Serov and Atanassov *et al.*, and offered by Pajarito Powder, USA.[19,42–45]

We now report a scalable, simple, decagram-scale synthesis of an active and stable Fe–N–C SAC for the ORR in acid ($E_{\frac{1}{2}}$ = 0.70 V *vs.* RHE). Our goal is to simplify the synthesis without losing activity, to allow researchers in academia and industry access to gram quantities of an efficient ORR catalyst. To this end, we successfully united two templating strategies in a single heat-treatment. The first strategy is active site imprinting, a novel approach towards well-defined, atomically-dispersed iron-nitrogen moieties in carbon electrocatalysts.[26,46,47] In this method, N-coordinated non-precious cations such as Mg^{2+} or Zn^{2+} can be embedded *via* N-coordination into a carbon surface during pyrolysis. Then, ion-exchange (transmetalation) with iron yields iron–nitrogen moieties, at temperatures low enough (80 °C) to prevent carbothermal reduction of iron and the undesirable generation of Fe(0) or Fe$_3$C phases.[46–49]

In parallel, in order to create a flow-enhancing hierarchical porosity, we relied on the self-templating strategy.[50–55] In this method, pyrolysis of a metal–organic coordination polymer yields a carbon skeleton embedded with metal oxide or carbonate particles; removal of the inorganic phases by simple washing leaves behind a heteroatom-doped, hierarchically porous carbon with a high specific surface area (SSA). Alkaline earth metals (Mg^{2+}, Ba^{2+}) are most commonly used for this application.[50,52–55] Iron itself, however, cannot be employed to yield single atom Fe–N–Cs directly, since carbothermal reduction of iron would result in inorganic iron phases as undesirable side products, leading to pore blocking[49] and corrosive Fenton activity.[56]

Thus, we took advantage the ability of Mg to act as a dual template, both imprinting active sites[46] and templating hierarchical porosity.[52–54] By pyrolyzing a novel and inexpensive magnesium iminodiacetate precursor, followed by washing and low-temperature transmetalation, we obtained a hierarchically porous, graphitized carbon, containing a significant proportion (43%) of desirable "surface Fe–N$_4$" (also called "D1") sites.[57–59] Moreover, the synthesis was successfully scaled-up from the hundred mg to over ten gram scale. We provide an active, stable, and scalable material with the potential to become a useful workhorse for academic and industrial research groups interested in PGM-free, hierarchically porous, atomically-dispersed ORR catalysts.

Results and discussion

Magnesium iminodiacetate (Mg-IDA), a metal–organic coordination polymer (MOCP), was precipitated in hot water from basic magnesium carbonate and iminodiacetic acid (NH(CH$_2$-COOH)$_2$, IDA) at a 1 : 1 molar ratio. During pyrolysis, the iminodiacetate ligand is carbonized into an N-doped carbon, while the magnesium carboxylates decompose to give MgO nanoparticles and CO_2.[60] Exothermic crystallization of MgO was observed by thermal gravimetric analysis between 750 and 1000 °C (Fig. S1†).[53,60] This temperature range is thus useful for pyrolysis, due to expected variations in the MgO particle sizes and degrees of agglomeration.[52–54] Mg-IDA was pyrolyzed at a range of temperatures ($T_{pyrolysis}$ = 800, 850, 900, 950 °C), resulting in fine black powders (denoted as Mg/NC_$T_{pyrolysis}$). The carbons are highly porous, foam-like, and dotted with bright particles, as seen by scanning electron microscopy (SEM, Fig. 1a). The particle sizes are in the 10–100 nm range, and are composed of crystalline MgO (powder X-ray diffraction, XRD, Fig. S2†). Scherrer analysis reveals typical coherent scattering lengths of 8–10 nm (Fig. S2,† inset). This is smaller than the particle size, indicating agglomeration and/or defects.[55] The MgO was removed by HCl washing, leaving behind a sponge-like, hierarchically porous morphology (Fig. 1b), expected to be beneficial for mass transport during electrocatalysis. Importantly, the carbon texture is robust across the 800–950 °C temperature range. Transmetalation was then carried out in an anhydrous methanolic solution of FeCl$_2$, under reflux at 80 °C. The resulting Fe–N–Cs are named [Fe(NC_$T_{pyrolysis}$)], adapting on the nomenclature used in coordination chemistry.

19860 | *J. Mater. Chem. A*, 2022, **10**, 19859–19867

This journal is © The Royal Society of Chemistry 2022
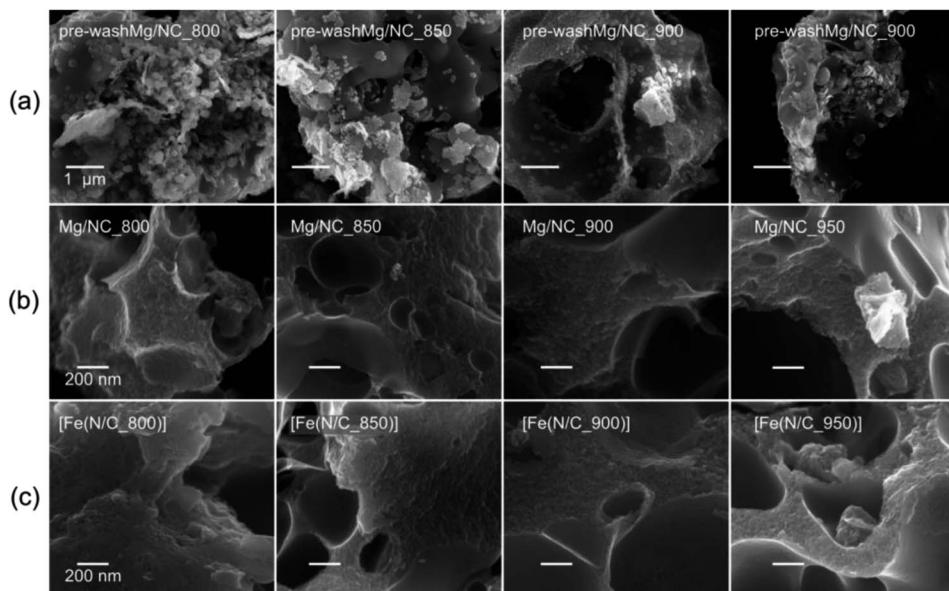
Fig. 1 Scanning electron micrographs of (a) MgO@NC as pyrolyzed, (b) Mg/NC after washing, (c) [Fe(N/C)] after transmetalation.

To quantify the hierarchical porosity, the carbons were characterized by N_2 physisorption porosimetry at 77 K, both before and after transmetalation (Fig. 2a–d). All isotherms belong to the H4 type.[61] A steep increase in gas uptake at low p/p_0 values reveals the presence of micropores (<2 nm). The subsequent slope, the indicated plateau, and desorption hysteresis arise from N_2 physisorption in mesopores (2–50 nm), while the further uptake at high p/p_0 values indicates additional macropores (>50 nm). The steep desorption at $p/p_0 \approx 0.4$ is characteristic for cavitation/blocking effects, indicating that the mesopores are connected via small bottlenecks.[61,62] All carbons

exhibit high SSAs and large total pore volumes (1100–1700 m^2 g^{-1}, Table 1), as calculated by Brunauer–Emmett–Teller (BET) theory. Both the high SSA values and the significant mesopore content make these carbons promising for mass transport during electrocatalysis. Pore size distributions, calculated from the adsorption isotherms using a quenched-solid DFT model for slit, cylindrical and spherical pores, shows three similar peaks in the carbons, centred at diameters of 1.0, 3.5 and 6.5 nm (Fig. 2e–h).

Importantly, the isotherms retain their shape following transmetalation, revealing that the ion exchange does not harm
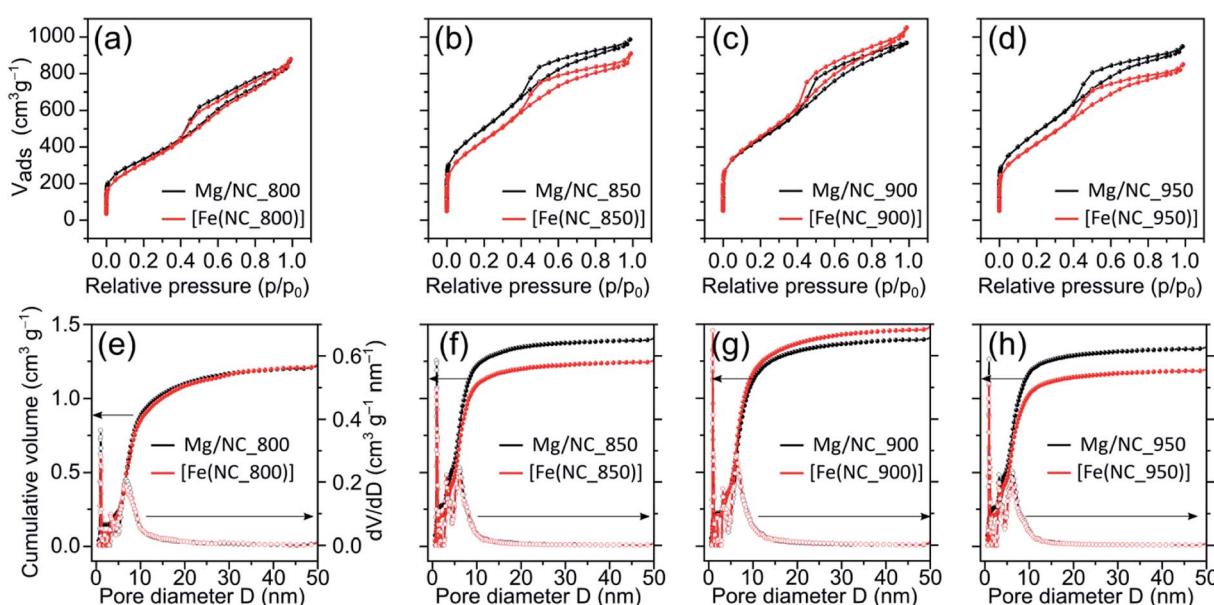
Fig. 2 (a)–(d) N_2 physisorption isotherms on Mg/NC (black) and [Fe(N/C)] (red) samples, pyrolyzed at different temperatures. (e)–(h) Cumulative and differential pore size distributions (QS-DFT model).

Table 1 Porosity analysis for Mg/NC and [Fe(N/C)] catalysts derived from N_2 sorption

Sample	SSA ($m^2 g^{-1}$)	S_{micro} ($m^2 g^{-1}$)	S_{meso} ($m^2 g^{-1}$)	V_{micro} ($cm^3 g^{-1}$)	V_{total} ($cm^3 g^{-1}$)
Mg/NC_800	1175	372	803	0.14	1.34
[Fe(N/C_800)]	1116	183	933	0.08	1.35
Mg/NC_850	1780	686	1094	0.27	1.52
[Fe(N/C_850)]	1569	477	1092	0.20	1.40
Mg/NC_900	1565	563	1002	0.22	1.49
[Fe(N/C_900)]	1614	471	1143	0.20	1.62
Mg/NC_950	1708	666	1042	0.25	1.46
[Fe(N/C_950)]	1496	505	991	0.20	1.31

the hierarchically porous morphology of the catalysts. The micropore surface area (S_{micro}) is reduced slightly (by 3–12%) following the ion-exchange, due to some blocking of micropores by residual iron oxides (see below). For [Fe(N/C_800)], [Fe(N/C_850)] and [Fe(N/C_950)] the characteristic pore sizes remain unchanged after transmetalation. Overall, the active site imprinting is orthogonal to the design of the hierarchically porosity of the carbon support.

To be active in electrocatalysis, carbons must be electrically conductive, which requires a sufficient degree of graphitization. The latter can be estimated by Raman spectroscopy, using the intensity ratio between the D band ($\nu = 1350$ cm^{-1}, typical of defects) and the G band ($\nu = 1580$ cm^{-1}, typical to graphitic regions).[53] All Mg/NC samples exhibit similar Raman spectra (Fig. 3), with graphitic domains ranging in length (L_a) between 13.4–14.4 nm (Table 2). This degree of graphitization indicates sufficient and similar conductivities in the material.[53,63]

Nitrogen surface functionalities play a key role in forming the active sites. X-ray photoelectron spectra (XPS) in the N 1s region were collected for the Mg–N–Cs, and deconvoluted into five different types of nitrogen (Fig. 4a–d): pyridinic (398.2–398.8 eV), metal-bound (399.4–400.0 eV), pyrrolic (400.1–400.5 eV), graphitic (401.2–401.5 eV) and oxidized nitrogen species (>403 eV).[64,65] The effect of pyrolysis temperature on the surface concentrations of nitrogen, carbon and oxygen is summarized in Table 2. The total surface nitrogen content is constant between 800 °C and 900 °C, and decreases at 950 °C. With increasing pyrolysis temperature, the proportion of edge-located nitrogen atoms (pyridinic, pyrrolic) decreases, and that of graphitic nitrogen increases. This reveals the lateral growth of graphitic nanostructures, and relates to enhanced

conductivity.[46,52,64] Metal–nitrogen bonds are found at the surface both before and after transmetalation, indicating the coordination of Mg^{2+} and then Fe^{2+} to nitrogen moieties. Following transmetalation, the N 1s spectra retain their general shape (Fig. 4e–h), as well as the surface concentration of graphitic nitrogen atoms (Table 2). The relative proportion of Me–N bonds rises with the pyrolysis temperature and peaks at 900 °C, indicating an optimal coordination environment at this temperature. Trace amounts of Mg (0.13–0.22 wt%) remain in the bulk of the acid washed material, as revealed by inductively coupled plasma mass spectrometry (ICP-MS, Table S1†), and supporting the case for a strong $Mg–N_4$ coordination.[66]

Finally, the robustness of the carbon composition along the pyrolysis was investigated by heating Mg/NC_800 in argon from room temperature to 950 °C in a thermogravimetric setup coupled to mass spectrometry (Fig. S3†). Following the initial steep mass decrease due to desorption of physisorbed gases, CO_2 signals ($m/z = 44, 45, 22$) and NO signals ($m/z = 30$) evolve only after 700 °C. This slow and steady loss of carboxylic and nitrogen groups corroborates the SEM observations that the carbons are not significantly changed over a broad pyrolysis range, and that their synthesis is robust.

[Fe(NC)_900] was selected for further analysis and tests, exhibiting the highest proportion of metal-bound nitrogens (24.4%) and the highest SSA (1614 $m^2 g^{-1}$). To observe the finest nanopores (<5 nm), high-resolution transmission electron microscopy (HR-TEM) was performed for Mg/NC_900 and [Fe(N/C_900)] (Fig. 5a and b). The carbon is homogeneously nanoporous, corroborating the hierarchical porosity, and promising fast flow to active sites during catalysis. The dispersion of nitrogen and iron dopants in the transmetalated sample
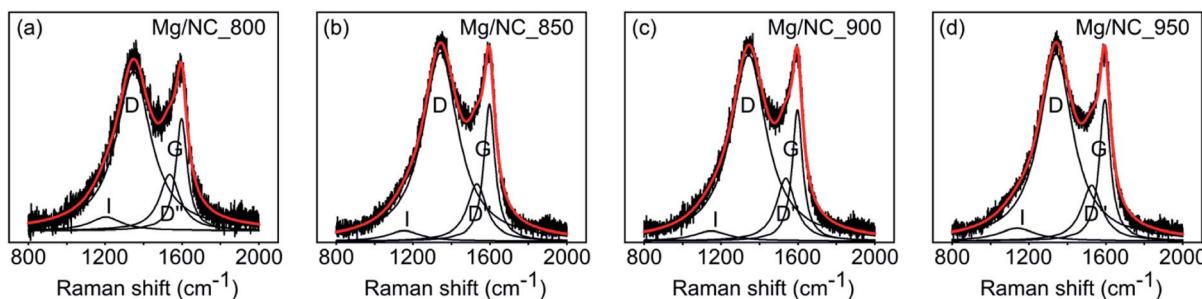
Fig. 3 Deconvoluted Raman spectra of the Mg/NC samples, pyrolyzed at different temperatures.

19862 | J. Mater. Chem. A, 2022, 10, 19859–19867

This journal is © The Royal Society of Chemistry 2022

Table 2 Chemical composition of the materials, as measured by XPS and Raman spectroscopies

Sample	Surface elemental composition (at%)			Surface nitrogen distribution (%)					Graphitization	
	C	N	O	Pyridinic	Pyrrolic	Metal-N	Graphitic	N–O	I_D/I_G	L_a^{67} (nm)
Mg/NC_800	87.90	6.61	5.49	35.92	30.38	18.17	11.85	3.69	1.4	13.7
[Fe(N/C)_800]	87.76	6.60	5.64	31.51	32.73	21.36	11.60	2.80		
Mg/NC_850	88.20	6.29	5.51	34.39	29.44	21.47	11.01	3.69	1.38	13.9
[Fe(N/C)_850]	87.16	6.04	6.81	31.11	28.05	25.95	10.60	4.28		
Mg/NC_900	89.44	6.78	3.77	31.95	24.53	23.63	14.50	5.39	1.43	13.4
[Fe(N/C)_900]	88.93	5.63	5.44	32.97	22.30	24.40	14.16	6.18		
Mg/NC_950	91.11	5.02	3.87	28.57	26.43	18.56	17.13	9.31	1.33	14.4
[Fe(N/C)_950]	90.06	4.81	5.12	30.00	23.28	23.73	17.10	5.89		

was mapped using a high angle annular dark field (HAADF) detector and energy dispersive X-ray spectroscopy (EDS) in scanning transmission electron microscopy (STEM) mode.[49,68] The micrographs reveal atomically dispersed Fe atoms, along with an even distribution of nitrogen atoms, overall revealing a successful ion-exchange process toward Fe–N–C SACs (Fig. 5c–f). Some Fe-based nanoparticles (2–4 nm) are also observed as side products of the transmetalation, albeit at a low concentration. Such iron-containing nanoparticles explain the slight decrease in micropore area that follows transmetalation (Table 1), as they likely block micropores.

To identify the iron species in [Fe(NC_900)], the sample was studied by Mössbauer spectroscopy at 4.2 K. Recently, room temperature measurements were shown to potentially cause overestimation of Fe–N_4 moieties, since oxidic iron nanoparticles/clusters may appear as doublets at room temperature.[47,69] Such oxidic nanoclusters reveal their characteristic magnetism in measurements at 4.2 K, where a magnetic hyperfine splitting can be observed because the particles are

magnetically ordered and superparamagnetic relaxations are blocked. The 4.2 K Mössbauer spectrum of [Fe(NC_900)] exhibits a sextet and two doublets (Fig. 6). The sextet is assigned to oxidic Fe nanoparticles, which may have formed through iron coordination with oxygen surface groups, or during the aqueous acid work-up that follows the transmetalation step. The two quadrupole doublets in the spectrum correspond to the doublets named D1 and D3 in the literature[47] according to their isomer shift and electric quadrupole interaction (Table S2†). The D3 doublets, typically arising from high spin Fe^{2+},[47] were reported in room temperature Mössbauer measurements of Fe–N–C electrocatalysts, but could not be correlated to ORR activity. In contrast, the intensity of the D1 doublets correlates positively with the ORR activity.[57–59] Importantly, D1 contributes as much as 43% to the total iron content of 0.8 wt% of the studied catalyst, which could be calculated from the total absorption of the Mössbauer spectrum (Tables S2–S4†), making [Fe(NC_900)] a promising electrocatalyst with many utilizable single atom catalytic sites.
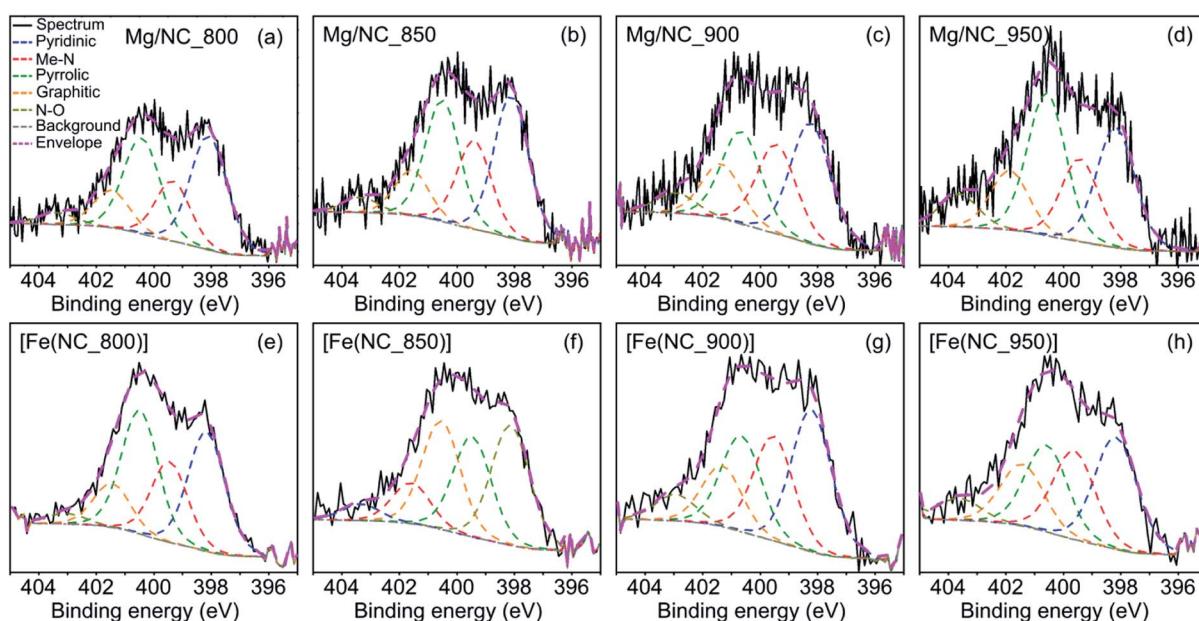
Fig. 4 Deconvoluted XPS spectra in the N 1s region, for the (a)–(d) Mg/NC and (e)–(h) [Fe(N/C)] samples.

This journal is © The Royal Society of Chemistry 2022

J. Mater. Chem. A, 2022, 10, 19859–19867 | **19863**
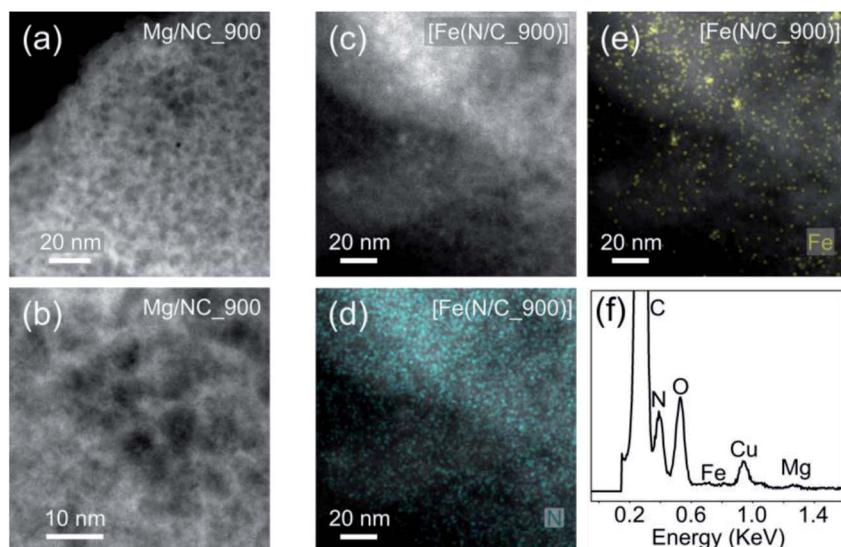
Fig. 5 HRTEM micrographs of (a) and (b) Mg/NC_900; (c) [Fe(N/C_900)]; HR-STEM mapping of (d) nitrogen and (e) iron in [Fe(N/C_900)]; (f) EDS spectrum of [Fe(N/C_900)].
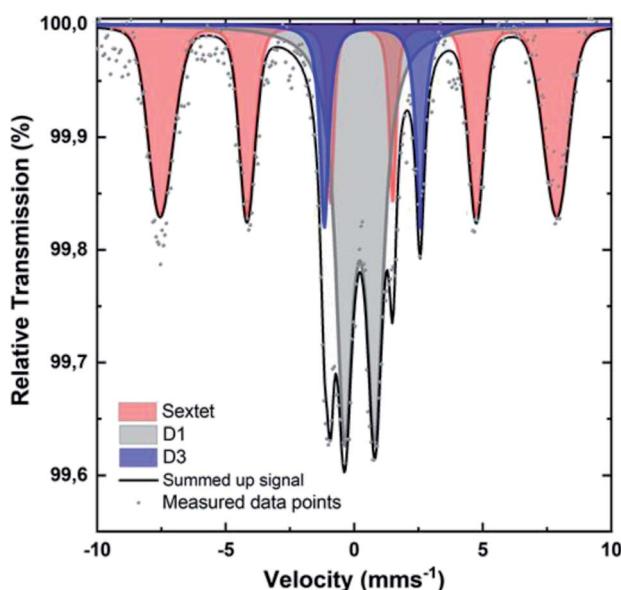

Fig. 6 Mössbauer spectrum of [Fe(N/C_900)] obtained at 4.2 K.

kinetics remain limiting over the potential range. Half-wave potentials ($E_{\frac{1}{2}}$), typical (though loading-dependent) ORR activity descriptors, ranged between 0.63–0.70 V vs. RHE (Table 3), indicating high ORR activity of these Fe–N–C electrocatalysts.[70] The mass activities extracted from LSV curves are similar to that of commercially available Fe–N–C catalysts.[71]

The stability of the carbon electrocatalysts towards corrosion was measured for [Fe(N/C_900)] by repeated cycling
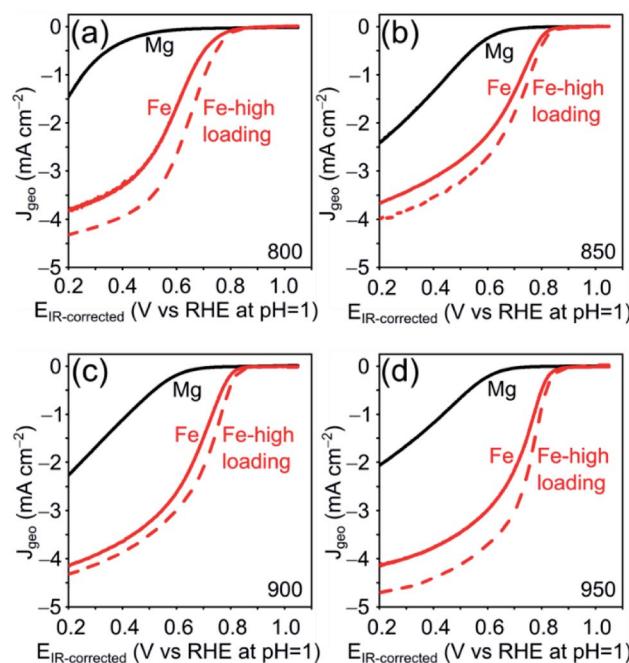

Fig. 7 ORR activities of Mg–N–C (200 µg cm^{-2}, black), Fe–N–C (200 µg cm^{-2}, red solid) and Fe–N–C (500 µg cm^{-2}, red dashed), following pyrolysis at four temperatures. LSVs in O$_2$-saturated 0.1 M HClO$_4$, rotating at 1600 rpm, scan rate 10 mV s^{-1}.

The electrocatalytic ORR activity of the obtained Fe–N–C was tested in a standard three electrode rotating disc electrode (RDE) setup in 0.1 M HClO$_4$ electrolyte and compared to the respective Mg/NCs. The thin-film electrodes were prepared by drop-casting, at catalyst loadings of 200 and 500 µg cm^{-2}. All four Mg/NC samples exhibited poor ORR activities: the linear sweep voltammograms (LSVs) show onset potentials of 0.7 V vs. RHE at pH = 1, and low current densities of 1.5–2.5 mA cm^{-2} at 0.2 V (Fig. 7). Transmetalation with iron improved the ORR activity drastically: the kinetic region is shifted positively by more than 300 mV, the onset potential increases to 0.83 V, and current densities at 0.2 V are in the range of 4 mA cm^{-2}. The

19864 | J. Mater. Chem. A, 2022, 10, 19859–19867

This journal is © The Royal Society of Chemistry 2022

Table 3 ORR activity descriptors of the Fe−N−C materials

Sample	$E_{\frac{1}{2}}$ (V)	I_m (A g^{-1}) at 0.8 V
[Fe(NCs)]_800	0.63	0.36 ± 0.10
[Fe(NCs)]_850	0.68	0.96 ± 0.12
[Fe(NCs)]_900	0.69	0.95 ± 0.04
[Fe(NCs)]_950	0.70	1.22 ± 0.11

experiments in an N$_2$-saturated electrolyte. Corrosive conditions at the cathode may be caused by the start-up and shut-down of PEM fuel cells.[72] The voltage was cycled between open circuit potential (OCP) and 1.4 V *vs.* RHE, revealing a small increase in double layer capacitance and pseudo-capacitive currents, and a slight decrease in current density after 1000 cycles (Fig. S4†).[73] For carbons with such large SSA (>1100 m^2 g^{-1}), relatively large pore sizes (>6 nm), and significant oxygen content (>5.44 at% in [Fe(NC_900)] by ICP-MS), this degradation is remarkably low, indicating that carbon corrosion is very moderate.

The hierarchically porous, atomically dispersed Fe−N−C electrocatalysts reported herein are also very easy to produce. To demonstrate the scalability of the synthesis, we carried out a five-fold increase in scale of the Mg-IDA precipitation, and then repeated the synthesis. A total of about 0.2 kg Mg-IDA was prepared. The next stages of the synthesis – pyrolysis at 900 °C, acid wash, drying and transmetalation in methanolic FeCl$_2$ solution – were done in two batches, yielding 25 g of MgO@NC_900 and finally 10.1 grams of [Fe(N/C_900)]. The Raman spectra and HRSEM micrographs are identical, revealing remarkably similar degrees of graphitization and porous microstructure (Fig. 8). The isotherms are similar in shape. The large batch carbon has a lower surface area (1323 *vs.* 1614 m^2 g^{-1}) and a higher gas uptake near $p = p_0$, suggesting a slightly higher degree of large meso- and small macropores. ICP-MS measurements reveal identical nitrogen content (7.8 and 7.6 wt% for the small and large batches, respectively). The

electrochemical activity of the batches is also similar (Table S4†), with identical onset potentials (0.84 ± 0.01) and half-wave potentials (0.69 ± 0.005).

Conclusions

We report a simple and scalable (decagram scale) synthesis of an atomically-dispersed, hierarchically porous Fe−N−C electrocatalyst for acidic ORR. Pyrolysis of magnesium iminodiacetate yielded Mg−N$_4$ sites that could later be transmetalated with iron ("active site imprinting"), as well as MgO nanoparticles and particle agglomerates that served as templates for meso- and macroporosity ("pore self-templating"). Thorough material characterization by XRD, HRSEM, HRTEM, XPS, Raman spectroscopy, N$_2$ sorption and Mössbauer spectroscopy at 4.2 K revealed the structure of the active sites (43% of the iron as surface-embedded Fe−N$_4$) and the flow-enhancing porosity of the carbon support. Rotating disk half-cell tests revealed half-wave potentials of 0.7 V *vs.* RHE in 0.1 M HClO$_4$, high mass activity, and high stability against carbon corrosion. The carbon could be scaled up by a factor of 100 very simply, while conserving the morphology and activity. The straightforward synthesis of the active ORR electrocatalyst provides simple access to reasonable amounts of single-atom Fe−N−C catalysts also for researchers not specialized in synthesis.

Conflicts of interest

There are no conflicts to declare.

Acknowledgements

Notes and references

1 F. Eljack and M.-K. Kazi, *Frontiers in Sustainability*, 2021, **1**, 14.
2 T. Yoshida and K. Kojima, *Electrochem. Soc. Interface*, 2015, **24**, 45.
3 Y. Manoharan, S. E. Hosseini, B. Butler, H. Alzhahrani, B. T. F. Senior, T. Ashuri and J. Krohn, *Appl. Sci.*, 2019, **9**, 2296.


Fig. 8 Comparing small batch (0.1 gr, black) and large batch (10.1 gr, red) syntheses of [Fe(N/C)_900]: (a) Raman spectra of Mg(N/C_900). (b) N$_2$ sorption isotherms of [Fe(N/C_900)]. (c) HRSEM micrographs of [Fe(NC_900)].

This journal is © The Royal Society of Chemistry 2022

J. Mater. Chem. A, 2022, **10**, 19859–19867 | **19865**

4 M. M. Whiston, I. L. Azevedo, S. Litster, K. S. Whitefoot, C. Samaras and J. F. Whitacre, *Proc. Natl. Acad. Sci. U. S. A.*, 2019, **116**, 4899–4904.

5 C. S. Gittleman, A. Kongkanand, D. Masten and W. Gu, *Curr. Opin. Electrochem.*, 2019, **18**, 81–89.

6 R. Jasinski, *Nature*, 1964, **201**, 1212–1213.

7 H. Jahnke, M. Schönborn and G. Zimmermann, in *Physical and Chemical Applications of Dyestuffs*, ed. F. P. Schäfer, H. Gerischer, F. Willig, H. Meier, H. Jahnke, M. Schönborn and G. Zimmermann, Springer, Berlin, Heidelberg, 1976, pp. 133–181.

8 S. Gupta, D. Tryk, I. Bae, W. Aldred and E. Yeager, *J. Appl. Electrochem.*, 1989, **19**, 19–27.

9 M. Lefèvre, E. Proietti, F. Jaouen and J.-P. Dodelet, *Science*, 2009, **324**, 71–74.

10 V. Glibin, G. Zhang, J.-P. Dodelet and S. Sun, *J. Electrochem. Soc.*, 2021, **168**, 094502.

11 K. Artyushkova, C. Walker, W. Patterson and P. Atanassov, *Electrocatalysis*, 2014, **5**, 241–247.

12 F. Luo, S. Wagner, I. Onishi, S. Selve, S. Li, W. Ju, H. Wang, J. Steinberg, A. Thomas, U. I. Kramm and P. Strasser, *Chem. Sci.*, 2021, **12**, 384–396.

13 H. Lee, M. J. Kim, T. Lim, Y.-E. Sung, H.-J. Kim, H.-N. Lee, O. J. Kwon and Y.-H. Cho, *Sci. Rep.*, 2017, **7**, 5396.

14 W. Sangkhun, J. Ponchai, C. Phawa, A. Pengsawang, K. Faungnawakij and T. Butburee, *ChemCatChem*, 2022, **14**, e202101266.

15 S. Akula, M. Mooste, B. Zulevi, S. McKinney, A. Kikas, H.-M. Piirsoo, M. Rähn, A. Tamm, V. Kisand, A. Serov, E. B. Creel, D. A. Cullen, K. C. Neyerlin, H. Wang, M. Odgaard, T. Reshetenko and K. Tammeveski, *J. Power Sources*, 2022, **520**, 230819.

16 C. Wan, X. Duan and Y. Huang, *Adv. Energy Mater.*, 2020, **10**, 1903815.

17 X. Xie, C. He, B. Li, Y. He, D. A. Cullen, E. C. Wegener, A. J. Kropf, U. Martinez, Y. Cheng, M. H. Engelhard, M. E. Bowden, M. Song, T. Lemmon, X. S. Li, Z. Nie, J. Liu, D. J. Myers, P. Zelenay, G. Wang, G. Wu, V. Ramani and Y. Shao, *Nat. Catal.*, 2020, **3**, 1044–1054.

18 L. Jiao, J. Li, L. L. Richard, Q. Sun, T. Stracensky, E. Liu, M. T. Sougrati, Z. Zhao, F. Yang, S. Zhong, H. Xu, S. Mukerjee, Y. Huang, D. A. Cullen, J. H. Park, M. Ferrandon, D. J. Myers, F. Jaouen and Q. Jia, *Nat. Mater.*, 2021, **20**, 1385–1391.

19 H. Adabi, A. Shakouri, N. Ul Hassan, J. R. Varcoe, B. Zulevi, A. Serov, J. R. Regalbuto and W. E. Mustain, *Nat. Energy*, 2021, **6**, 834–843.

20 H. Zhang, H. T. Chung, D. A. Cullen, S. Wagner, U. I. Kramm, K. L. More, P. Zelenay and G. Wu, *Energy Environ. Sci.*, 2019, **12**, 2548–2558.

21 J. Li, L. Jiao, E. Wegener, L. L. Richard, E. Liu, A. Zitolo, M. T. Sougrati, S. Mukerjee, Z. Zhao, Y. Huang, F. Yang, S. Zhong, H. Xu, A. J. Kropf, F. Jaouen, D. J. Myers and Q. Jia, *J. Am. Chem. Soc.*, 2020, **142**, 1417–1423.

22 M. Primbs, Y. Sun, A. Roy, D. Malko, A. Mehmood, M.-T. Sougrati, P.-Y. Blanchard, G. Granozzi, T. Kosmala, G. Daniel, P. Atanassov, J. Sharman, C. Durante, A. Kucernak, D. Jones, F. Jaouen and P. Strasser, *Energy Environ. Sci.*, 2020, **13**, 2480–2500.

23 J. Yoon, S. Kim, H. Park, K. Prabakar and O. Lun Li, *Mater. Lett.*, 2021, **291**, 129561.

24 Y. Zhou, Y. Yu, D. Ma, A. C. Foucher, L. Xiong, J. Zhang, E. A. Stach, Q. Yue and Y. Kang, *ACS Catal.*, 2021, **11**, 74–81.

25 Q. Qu, S. Ji, Y. Chen, D. Wang and Y. Li, *Trends Chem.*, 2021, **3**, 954–968.

26 D. Menga, J. L. Low, Y.-S. Li, I. Arčon, B. Koyutürk, F. Wagner, F. Ruiz-Zepeda, M. Gaberšček, B. Paulus and T.-P. Fellinger, *J. Am. Chem. Soc.*, 2021, **143**, 18010–18019.

27 J. Fan, M. Chen, Z. Zhao, Z. Zhang, S. Ye, S. Xu, H. Wang and H. Li, *Nat. Energy*, 2021, **6**, 475–486.

28 H. Sun, J. Zhu, D. Baumann, L. Peng, Y. Xu, I. Shakir, Y. Huang and X. Duan, *Nat. Rev. Mater.*, 2019, **4**, 45–60.

29 S. Fu, C. Zhu, D. Su, J. Song, S. Yao, S. Feng, M. H. Engelhard, D. Du and Y. Lin, *Small*, 2018, **14**, 1703118.

30 G. Zhang, Y. Jia, C. Zhang, X. Xiong, K. Sun, R. Chen, W. Chen, Y. Kuang, L. Zheng, H. Tang, W. Liu, J. Liu, X. Sun, W.-F. Lin and H. Dai, *Energy Environ. Sci.*, 2019, **12**, 1317–1325.

31 Y. Wang, Q. Li, L. Zhang, Y. Wu, H. Chen, T. Li, M. Xu and S.-J. Bao, *J. Mater. Chem. A*, 2021, **9**, 7137–7142.

32 T. Chen, J. Wu, C. Zhu, Z. Liu, W. Zhou, C. Zhu, C. Guan and G. Fang, *Chem. Eng. J.*, 2021, **405**, 125956.

33 Y. Deng, B. Chi, X. Tian, Z. Cui, E. Liu, Q. Jia, W. Fan, G. Wang, D. Dang, M. Li, K. Zang, J. Luo, Y. Hu, S. Liao, X. Sun and S. Mukerjee, *J. Mater. Chem. A*, 2019, **7**, 5020–5030.

34 F. Jaouen, J. Herranz, M. Lefèvre, J.-P. Dodelet, U. I. Kramm, I. Herrmann, P. Bogdanoff, J. Maruyama, T. Nagaoka, A. Garsuch, J. R. Dahn, T. Olson, S. Pylypenko, P. Atanassov and E. A. Ustinov, *ACS Appl. Mater. Interfaces*, 2009, **1**, 1623–1639.

35 M. P. Oyarzún, N. Silva, D. Cortés-Arriagada, J. F. Silva, I. O. Ponce, M. Flores, K. Tammeveski, D. Bélanger, A. Zitolo, F. Jaouen and J. H. Zagal, *Electrochim. Acta*, 2021, **398**, 139263.

36 X. Yin, H. T. Chung, U. Martinez, L. Lin, K. Artyushkova and P. Zelenay, *J. Electrochem. Soc.*, 2019, **166**, F3240.

37 A. Serov, K. Artyushkova, E. Niangar, C. Wang, N. Dale, F. Jaouen, M.-T. Sougrati, Q. Jia, S. Mukerjee and P. Atanassov, *Nano Energy*, 2015, **16**, 293–300.

38 A. Serov, M. J. Workman, K. Artyushkova, P. Atanassov, G. McCool, S. McKinney, H. Romero, B. Halevi and T. Stephenson, *J. Power Sources*, 2016, **327**, 557–564.

39 M. David, S. M. Lyth, R. Lindner and G. F. Harrington, in *Future-Proofing Fuel Cells*, Springer, 2021, pp. 35–56.

40 H. Yang, L. Shang, Q. Zhang, R. Shi, G. I. N. Waterhouse, L. Gu and T. Zhang, *Nat. Commun.*, 2019, **10**, 4585.

41 L. Zhao, Y. Zhang, L.-B. Huang, X.-Z. Liu, Q.-H. Zhang, C. He, Z.-Y. Wu, L.-J. Zhang, J. Wu, W. Yang, L. Gu, J.-S. Hu and L.-J. Wan, *Nat. Commun.*, 2019, **10**, 1–11.

42 A. Serov, K. Artyushkova, N. I. Andersen, S. Stariha and P. Atanassov, *Electrochim. Acta*, 2015, **179**, 154–160.

43 Q. Jia, N. Ramaswamy, U. Tylus, K. Strickland, J. Li, A. Serov, K. Artyushkova, P. Atanassov, J. Anibal, C. Gumeci,

19866 | *J. Mater. Chem. A*, 2022, **10**, 19859–19867

This journal is © The Royal Society of Chemistry 2022

S. C. Barton, M.-T. Sougrati, F. Jaouen, B. Halevi and S. Mukerjee, *Nano Energy*, 2016, **29**, 65–82.

44 World Intellectual Property Organization, WO2016133921A1, 2016.

45 A. Serov and P. Atanassov, *US Pat.*, US9673456B2, United States, 2017.

46 A. Mehmood, J. Pampel, G. Ali, H. Y. Ha, F. Ruiz-Zepeda and T.-P. Fellinger, *Adv. Energy Mater.*, 2018, **8**, 1701771.

47 D. Menga, F. Ruiz-Zepeda, L. Moriau, M. Šala, F. Wagner, B. Koyutürk, M. Bele, U. Petek, N. Hodnik, M. Gaberšček and T.-P. Fellinger, *Adv. Energy Mater.*, 2019, **9**, 1902412.

48 B. Koyutürk, Towards the Scalable Synthesis of PGM-free Catalysts for Oxygen Reduction Reaction, PhD thesis, Technischen Universität München, 2020.

49 T. Y. Burshtein, D. Aias, J. Wang, M. Sananis, E. M. Farber, O. M. Gazit, I. Grinberg and D. Eisenberg, *Phys. Chem. Chem. Phys.*, 2021, **23**, 26674–26679.

50 M. Inagaki, H. Orikasa and T. Morishita, *RSC Adv.*, 2011, **1**, 1620–1640.

51 G. A. Ferrero, M. Sevilla and A. B. Fuertes, *Carbon*, 2015, **88**, 239–251.

52 D. Eisenberg, W. Stroek, N. J. Geels, C. S. Sandu, A. Heller, N. Yan and G. Rothenberg, *Chem.–Eur. J.*, 2016, **22**, 501–505.

53 D. Eisenberg, P. Prinsen, N. J. Geels, W. Stroek, N. Yan, B. Hua, J.-L. Luo and G. Rothenberg, *RSC Adv.*, 2016, **6**, 80398–80407.

54 E. M. Farber, K. Ojha, T. Y. Burshtein, L. Hasson and D. Eisenberg, *Mater. Adv.*, 2020, **1**, 20–33.

55 E. M. Farber, K. Ojha, T. Y. Burshtein and D. Eisenberg, *J. Electrochem. Soc.*, 2020, **167**, 064517.

56 Á. García, L. Pascual, P. Ferrer, D. Gianolio, G. Held, D. C. Grinter, M. A. Peña, M. Retuerto and S. Rojas, *J. Power Sources*, 2021, **490**, 229487.

57 T. Mineva, I. Matanovic, P. Atanassov, M.-T. Sougrati, L. Stievano, M. Clémancey, A. Kochem, J.-M. Latour and F. Jaouen, *ACS Catal.*, 2019, **9**, 9359–9371.

58 U. I. Kramm, I. Herrmann-Geppert, P. Bogdanoff and S. Fiechter, *J. Phys. Chem. C*, 2011, **115**, 23417–23427.

59 U. I. Koslowski, I. Abs-Wurmbach, S. Fiechter and P. Bogdanoff, *J. Phys. Chem. C*, 2008, **112**, 15356–15366.

60 J. S. Budkuley and G. K. Naik, *Thermochim. Acta*, 1998, **320**, 115–120.

61 M. Thommes, K. Kaneko, A. V. Neimark, J. P. Olivier, F. Rodriguez-Reinoso, J. Rouquerol and K. S. W. Sing, *Pure Appl. Chem.*, 2015, **87**, 1051–1069.

62 M. Thommes, *Chem. Ing. Tech.*, 2010, **82**, 1059–1073.

63 M. Ghazinejad, S. Holmberg, O. Pilloni, L. Oropeza-Ramos and M. Madou, *Sci. Rep.*, 2017, **7**, 16551.

64 K. Artyushkova, *J. Vac. Sci. Technol., A*, 2020, **38**, 031002.

65 H. F. Gorgulho, F. Gonçalves, M. F. R. Pereira and J. L. Figueiredo, *Carbon*, 2009, **47**, 2032–2039.

66 D. Eisenberg, T. K. Slot and G. Rothenberg, *ACS Catal.*, 2018, **8**, 8618–8629.

67 M. B. Vázquez-Santos, E. Geissler, K. László, J.-N. Rouzaud, A. Martínez-Alonso and J. M. D. Tascón, *J. Phys. Chem. C*, 2012, **116**, 257–268.

68 W. Liu, L. Zhang, X. Liu, X. Liu, X. Yang, S. Miao, W. Wang, A. Wang and T. Zhang, *J. Am. Chem. Soc.*, 2017, **139**, 10790–10798.

69 S. Wagner, H. Auerbach, C. E. Tait, I. Martinaiou, S. C. N. Kumar, C. Kübel, I. Sergeev, H.-C. Wille, J. Behrends, J. A. Wolny, V. Schünemann and U. I. Kramm, *Angew. Chem., Int. Ed.*, 2019, **58**, 10486–10492.

70 D. E. Beltrán and S. Litster, *ACS Energy Lett.*, 2019, **4**, 1158–1161.

71 A. M. Damjanović, B. Koyutürk, Y.-S. Li, D. Menga, C. Eickes, H. A. El-Sayed, H. A. Gasteiger, T.-P. Fellinger and M. Piana, *J. Electrochem. Soc.*, 2021, **168**, 114518.

72 T. Mittermeier, A. Weiß, F. Hasché, G. Hübner and H. A. Gasteiger, *J. Electrochem. Soc.*, 2016, **164**, F127.

73 F. Forouzandeh, X. Li, D. W. Banham, F. Feng, S. Ye and V. Birss, *J. Electrochem. Soc.*, 2018, **165**, F3230.

This journal is © The Royal Society of Chemistry 2022

J. Mater. Chem. A, 2022, **10**, 19859–19867 | **19867**